Article:
Yang, J. orcid.org/0009-0003-2249-8030, Xiong, L., Wang, C. et al. (4 more authors) (2025) Selective synthesis of ethane from methane by a photocatalytic chemical cycle process. Advanced Energy Materials, 15 (9). 2404202. ISSN 1614-6832

https://doi.org/10.1002/aenm.202404202

ADVANCED ENERGY MATERIALS
www.advenergymat.de

Selective Synthesis of Ethane from Methane by a Photocatalytic Chemical Cycle Process

*Jianlong Yang, Lunqiao Xiong, Chao Wang, Lei Luo, Liqiang Jing, Natalia Martsinovich, and Junwang Tang**

Synthesis of value-added chemicals from methane remains a great challenge due to its high energy requirement, low conversion efficiency, and unavoidable over-oxidation of desired products. Here, the integration of a photon-driven chemical cycle process with a continuous flow reactor over the $Co_{0.2}Pd_{1.8}$-TiO_2 catalyst has led to the continuous synthesis of C_2H_6 from CH_4 with ≈100% selectivity under ambient conditions, simultaneously avoiding mixing flammable gas methane with O_2 for the chemicals production. Such high selectivity and activity are due to the active lattice oxygen of PdO_L and the oxygen-lean condition characterized in the chemical cycle, together with Co single atoms for the regeneration of the photocatalyst surface during the chemical cycle process. The consumed oxygen in PdO_L can be compensated by air during the subsequent catalyst regeneration process, leading to the stable activity during a 43 cycles test. Furthermore, this work to some extent demonstrates that the chemical cycle process not only improves the technoeconomic viability but also enhances safety of the process.

1. Introduction

The predicted reserves of shale gas and methane hydrate are so huge that methane (CH_4) is widely regarded as the most abundant building block for future chemical synthesis[1] On the other hand, accidental emissions of CH_4 can cause serious environmental issues. It is thus highly desirable to develop a sustainable and green solution to efficiently synthesize high-value chemicals from methane. However, reactions converting CH_4 molecule to value-added products are rather challenging due to its high C–H bond enthalpy (439 kJ·mol^{-1}), low polarizability (2.84×10^{-40} C^2·m^2·J^{-1}), and negligible proton affinity (544 kJ·mol^{-1}). Currently, industrial transformation of CH_4 relies on indirect processes, e.g. the steam reforming process followed by Fischer–Tropsch technology, which requires high operating temperature and pressure to overcome the reaction barriers, and leads to large amounts of CO_2 emission.[2]

The direct coupling routes to convert CH_4 into C_2 products are highly economically attractive, but they remain challenging chemical processes. It is well known that methane conversion to C_1 only involves C-H bond activation, while methane to C_2 requires a catalyst not only to activate the C-H bond but more importantly to promote C-C coupling. These routes can be classified into two categories: the non-oxidative coupling route and the oxidative coupling route. The non-oxidative

J. Yang, L. Xiong, J. Tang
Industrial Catalysis Center
Department of Chemical Engineering
Tsinghua University
Beijing 100084, P. R. China
E-mail: jwtang@tsinghua.edu.cn

J. Yang, L. Luo
Key Lab of Synthetic and Natural Functional Molecule Chemistry of Ministry of Education
The Energy and Catalysis Hub
College of Chemistry and Materials Science
Northwest University
Xi'an 710127, P. R. China

J. Yang
Yulin Innovation Institute of Clean Energy
Yulin 719000, P. R. China

C. Wang, J. Tang
Department of Chemical Engineering
University College London
Torrington Place, London WC1E 7JE, UK

L. Jing
Key Laboratory of Functional Inorganic Materials Chemistry (Ministry of Education)
School of Chemistry and Materials Science
Heilongjiang University
Harbin 150080, P. R. China

N. Martsinovich
Department of Chemistry
University of Sheffield
Brook Hill, Sheffield S3 7HF, UK

The ORCID identification number(s) for the author(s) of this article can be found under https://doi.org/10.1002/aenm.202404202

DOI: 10.1002/aenm.202404202

coupling of CH_4 (NOCM) demonstrates an atom utilization efficiency close to 100%, but suffers from unfavorable thermodynamics (ΔG^0 = 68.6 kJ mol^{-1}), resulting in a comparatively slower reaction rate. Furthermore, under oxygen-free conditions, coke accumulation could occur as a thermodynamically more favorable process (ΔG^0 = 50.7 kJ/mol), leading to fast catalyst deactivation.[3] For example, a well-designed TiO_2-loaded Pt single-atom nest was utilized for NOCM, achieving a C_2H_6 yield of 3.77 μmol h^{-1}.[4] In addition, the selectivity remains a challenge in this process, and it increases capital investment and energy costs associated with gas separation units required for the removal of other by-products, together with a carbon economy.

In contrast, the oxidative coupling of methane route (OCM) is thermodynamically favorable due to the participation of active oxidants (such as O_2, H_2O_2, and N_2O). However, the presence of these oxidants also leads to unavoidable peroxidation, resulting in low carbon utilization efficiency and undesirable carbon emissions besides safety issues.

The chemical cycle mechanism is widely used in combustion, which decouples a chemical reaction into consecutive reduction and oxidation reactions in the reactors. The key of a chemical cycle process is that the metal oxide releases reactive oxygen atoms from its lattice in the controlled manner. The released lattice oxygen is consumed in oxidation reactions as an oxidant and is reintroduced via re-oxidation cycling.[5] Thus the first step of the chemical cycle process resembles NCOM for methane activation due to a O_2-free environment and can readily control the degree of the partial oxidation of CH_4 while avoiding overoxidation by modulating the oxidation states of the metal oxide used.[6] There are a few examples in thermal catalytic conversion of CH_4 operated at high temperature to validate the efficiency of this process to achieve a high selectivity by avoiding overoxidation. For example, it was reported that $Na_2WO_4/FeMnO_3$ converted CH_4 to C_2-C_3 via a thermal catalytic chemical cycle system at 800 °C with a selectivity of 80%.[7] The excellent selectivity was attributed to the $FeMnO_3 \leftrightarrow [MnFe_2O_4 + MnO]$ redox cycle.

Semiconductor-based photocatalysis is an attractive technology to realize thermodynamically unfavorable reactions to take place at low temperature,[8] even at room temperature.[9] CH_4 conversion in the absence of active oxidants (including O_2, H_2O_2, and N_2O) is such a thermodynamically challenging reaction, while it can possibly be driven by photocatalysis even operated at room temperature, where C–H bond can be easily cleaved by photogenerated active species.[10] Integrating chemical cycle and photocatalysis may combine the advantages of both sides, achieving highly selective and efficient conversion of CH_4 under rather mild conditions to more valuable C_2 products (involving C-C coupling). Recently, an excellent report introduced photocatalysis in the chemical cycle process, achieving a moderate C_2H_6 yield of 2.3 μmol h^{-1} (or 23 μmol·g^{-1}·h^{-1}) and a selectivity of 82% at room temperature.[11]

TiO_2, particularly anatase TiO_2, which exhibits stronger photocatalytic activity compared to rutile TiO_2 and brookite TiO_2 phases in many reactions, has been regarded as the most stable and cost-effective photocatalyst for various chemical processes. However, it still suffers from slow charge separation and the over-oxidation of desired products.[12] This can be solved by loading transition metals (e.g., Co, Ni, Cu, Au, Pd, and Pt) that can serve as the acceptor of electrons or holes, thereby improving the photogenerated charge separation of TiO_2, leading to a high conversion.[13] More importantly, if the loaded transition metals can be coupled into a chemical cycle process, the overoxidation of desired products could be alleviated as the amount and oxidizing ability of the active species in the chemical cycle process could be subtly tuned.[6]

Here, we synthesized the very active $Co_{0.2}Pd_{1.8}$-TiO_2 catalyst and for the first time combined the photon-driven chemical cycle pathway with a flow process. Then the photon-driven chemical cycle flow process in the absence of O_2 has been successfully employed for C_2H_6 synthesis from CH_4 at room temperature. The yield of C_2H_6 reaches up to 74 μmol·g^{-1}·h^{-1} (or 3.7 μmol·h^{-1}) with a selectivity of nearly 100%, both are much higher than the previous NOCM results. Comprehensive characterizations including XPS, DRIFT and in situ EPR techniques etc. reveal that PdO_L is directly involved in the C-H bond breaking, accomplished by the consumption of its lattice oxygen (O_L) to form ·CH_3 and ·OH. The combination of the ·CH_3 radicals leads to extremely high selectivity to C_2H_6 in the oxygen-lean environment. Moreover, Co single atoms can promote the reduction reaction and remove the protons on the surface of the photocatayst, benefiting the controllable conversion of CH_4.[14] The consumed O_L is also replenished by O_2 gas in the subsequent catalyst regeneration process, completing the chemical cycle process. In addition, this chemical cycle process avoids mixing the flammable gas CH_4 with O_2 for chemicals production, promising arather safe continuous chemical process.

2. Results and Discussion

2.1. Photocatalytic Coupling of Methane

PdO_L was loaded over TiO_2 by the photodeposition method. The photocatalytic activity of prepared catalysts was tested for CH_4 conversion in a top-irradiated flow reactor, with a 365 nm LED as the light source (Figure S1, Supporting Information). The prepared catalyst film was placed on the copper grid of a reactor with a temperature probe to monitor the reaction temperature. CH_4 conversion on rutile TiO_2, anatase TiO_2, and Pd modified anatase TiO_2 was first compared. As shown in Figure S2 (Supporting Information), only C_2H_6 and H_2 are detected in the products. The photocatalytic activity of rutile TiO_2 is only half that of anatase TiO_2 (0.1 μmol h^{-1} in Figure S2, Supporting Information). The initial C_2H_6 production rate is significantly improved after loading Pd on anatase TiO_2 (up to 2.8 μmol h^{-1}). These results indicate that loading Pd on TiO_2 can effectively improve the CH_4 conversion activity. However, the stability of $Pd_{1.8}$-TiO_2 is very poor. As shown in Figure S3 (Supporting Information), the yield of C_2H_6 drops to 16% at 60 min, consistent with the previous results in a batch reactor.[11] This loss of activity is attributed to the substantial consumption of O_L of PdO_L under oxygen-lean conditions, and coking might start as reported in the conventional NOCM.[15] To precisely determine the reaction type and investigate the inactivation mechanism, the ratio of produced C_2H_6 to H_2 was then analyzed. As mentioned earlier, the direct coupling routes of CH_4 conversion can be classified into two categories: the non-oxidative coupling route (NOCM) and the oxidative coupling route. Since the reaction is conducted under O_2-free conditions, O_L is the only possible oxidant to participate in the methane

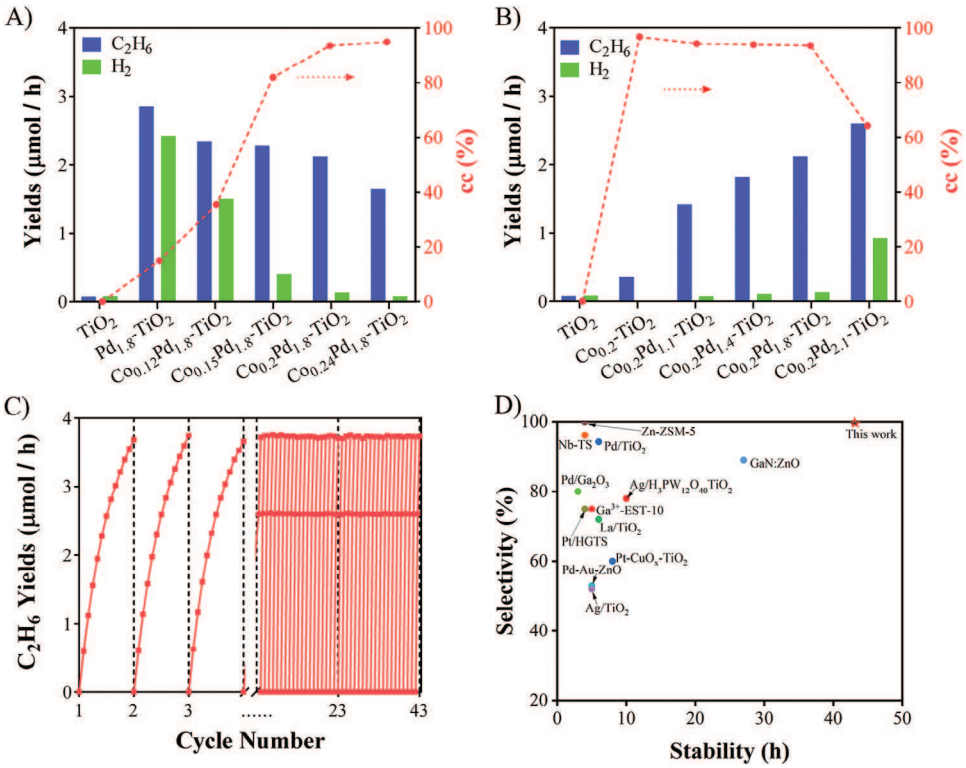

Figure 1. Photocatalytic CH_4 conversion over various catalysts. Initial CH_4 conversion to two products C_2H_6 and H_2 for a continuous run for half an hour and degree of chemical cycle process (cc %) over A) $Co_xPd_{1.8}$-TiO_2 and B) $Co_{0.2}Pd_y$-TiO_2. (Where x and y represent the mass percentages of Co and Pd to the TiO_2 substrate. x = 0, 0.12, 0.15, 0.2, 0.24 wt. %, y = 0, 1.1, 1.4, 1.8, 2.1 wt. %). cc (%) represents the proportion of the chemical cycle in the total CH_4 conversion reaction. The activity reported in the flow system was calculated by an integration of temporal yield over reaction time (reaction condition: 50 ml min^{-1} CH_4, 365 nm LED, 50 mg catalyst, 0.1 MPa). C) The C_2H_6 yields over the optimized $Co_{0.2}Pd_{1.8}$-TiO_2 recorded for 43 1-hour chemical cycles (reaction condition: 50 ml min^{-1} CH_4, 365 nm LED, 50 mg catalyst, 0.4 MPa). D) Representative works on photocatalytic CH_4 conversion to C_2H_6. The abscissa represents the results of sample stability testing, expressed in units of cycling number or operating time.

conversion reaction. If the O_L could be compensated later by a regeneration process (which will be confirmed later in this paper), then this route is a chemical cycle process. In the chemical cycle process, because O_L is involved in the reaction, the reduction product is H_2O instead of H_2 (Equation (1)). On the other hand, if NOCM takes place, the ratio of yielded C_2H_6 to H_2 should be 1, according to Equation (2).

$$2\,CH_4 + O_L \rightarrow C_2H_6 + H_2O \quad (1)$$

$$2\,CH_4 \rightarrow C_2H_6 + H_2 \quad (2)$$

One can see in Figure S2 (Supporting Information) that the initial yield of C_2H_6 is larger than that of H_2 and the ratio of C_2H_6 to H_2 is larger than 1 for the majority of the photocatalysts used, it suggests that the NOCM and complete chemical cycle coexist and they compete in the process. The proportion of chemical cycle (chemical cycle %) could be calculated via Equation (3).

$$\text{chemical cycle}\,\% = \frac{n\left(C_2H_6\right) - n\left(H_2\right)}{n\left(C_2H_6\right)} \quad (3)$$

As shown in Figure S4A (Supporting Information), dry air was then pumped into the system under light irradiation to compensate for the consumed O_L. The activity shows a moderate recovery first, but finally becomes inactive after 4 cycles. As shown in Figure S4B (Supporting Information), the appearance of $Pd_{1.8}$-TiO_2 turns brown after four cycles of reactions. This phenomenon suggests that the loss of activity may stem from carbon deposition obstructing active sites (similar to NOCM) or from the insufficient replenishment of consumed lattice oxygen.

As mentioned earlier, Co could promote the production of PdO_L, thereby introducing more O_L into Pd species.[14] Co single atoms and PdO_L were then co-loaded on TiO_2 by a two-step method. The prepared photocatalysts are named as Co_xPd_y-TiO_2 according to the weight percentage of Co and Pd to the TiO_2 substrate, which was analyzed by the inductively coupled plasma atomic emission spectroscopy (ICP-AES). The results of photocatalytic activity over a series of $Co_xPd_{1.8}$-TiO_2 are shown in **Figure 1**A. Increasing Co content in $Co_xPd_{1.8}$-TiO_2 results in decreased yields of both C_2H_6 and H_2, while the proportion of chemical cycle increases from 15% to 95%; more importantly, the long-time stability is increased, as discussed below. The catalyst with 0.2% Co content maintains high chemical cycle % and excellent activity.

To further optimize the catalytic activity, different amounts of Pd were loaded on TiO_2 while keeping the content of Co constant (0.2%), the results are shown in Figure 1B. The increase of Pd content results in an increase in the C_2H_6 production rate, while the proportion of chemical cycle decreases when the Pd

amount is over 1.8%, which is detrimental to the stability of the catalyst. The sample of $Co_{0.2}Pd_{1.8}$-TiO_2 well balances the activity and high chemical cycle ratio, thus is selected as the optimized composition for the following experiments. The product distrbution over $Co_{0.2}Pd_{1.8}$-TiO_2 by a OCM process with O_2 as the oxidant was also investigated. Two gases, CH_4 (20% CH_4 and 80% N_2) and O_2 (2% O_2 and 98% N_2), contributing to a total flow rate of 50 mL mi^{-1}n, were supplied to the reactor at different ratios (CH_4:O_2 = 4:1, 9:1, 24:1 and pure CH_4). As shown in Figure S5 (Supporting Information), the yield of C_2H_6 is 26.6 μmol h^{-1}, while the selectivity of C_2H_6 is only 49.4% when the ratio of CH_4 to O_2 is 4:1. As the CH_4 to O_2 ratio increases, the yield of C_2H_6 changes to 33.2, 16.1, and 1.5 μmol h^{-1} for the ratios of 9:1, 24:1 and pure CH_4 respectively. Meanwhile, the selectivity of the C_2H_6 exhibits an increasing trend, with the values of 79.9%, 91.3%, and nearly 100% for ratios of 9:1, 24:1, and pure CH_4, respectively. The above results suggest that even a small amount of O_2 enhances the photocatalytic activity over $Co_{0.2}Pd_{1.8}$-TiO_2, but large amount causes severe overoxidation. This overoxidation leads to significant CO_2 production, increasing capital investment and energy costs associated with gas separation units for the removal of other by-products, besides reduced carbon economy. This is a disadvantage of the OCM compared with the chemical cycle process. Moreover, changing the reaction pressure from 0.1, 0.2, 0.3, to 0.4 MPa reveals an enhanced yield of C_2H_6 (Figure S6, Supporting Information). For safety reasons, we did not increase the pressure in the system further. Specifically, the C_2H_6 yield rate over $Co_{0.2}Pd_{1.8}$-TiO_2 under 0.4 MPa drops to 30% after 60 minutes, which is used as an indicator for the regeneration of the oxide (Figure S7, Supporting Information). To replenish O_L of PdO_L, $Co_{0.2}Pd_{1.8}$-TiO_2 catalyst is regenerated in dry air under UV irradiation for 5 minutes (Figure 1C). The regenerated catalyst presents a similar activity to the as-prepared one, thus confirming the successful refill of O_L to achieve a complete chemical cycle process. The $Co_{0.2}Pd_{1.8}$-TiO_2 catalyst shows excellent stability over 43 cycles (conversion of CH_4 first and then the catalyst regeneration as shown in Figure 1C; Figure S8, Supporting Information). No CO_2 is detected during the methane conversion process. In this work, a flow process was employed to couple the methyl radicals generated during the first step to form ethane that is rapidly removed from the reactor to prevent product accumulation and potential overoxidation. Additionally, little CO_2 is produced during the catalyst regeneration process (Figure S9, Supporting Information), likely resulting from the oxidation of adsorbed methane and/or other hydrocarbons on the catalyst surface under oxygen-rich conditions. The calibration curve for CO_2 quantification shows excellent linearity with a coefficient higher than 0.99, and the detection limit of the current system is ≈20 ppm (Figure S10, Supporting Information). The apparent quantum yield (AQY) of this process is calculated to be 0.19%, which is significantly higher than the reported results from NOCM. For instance, the benchmark catalyst Pt/Ga-TiO_2-SiO_2 achieves an AQY of only 0.01%,[16] and even in the OCM on Pd-Bi/Ga_2O_3 an AQY of 0.2% was reported.[17] Compared with the reported photocatalysts, the well-designed $Co_{0.2}Pd_{1.8}$-TiO_2 catalyst exhibits unprecedented CH_4 conversion (Figure 1D) in terms of the selectivity and stability (detailed data are shown in Table S1, Supporting Information). Several control experiments were conducted to prove the necessity of a catalyst, CH_4 gas, and light for ethane production in the reaction system. The results in the Table S2 (Supporting Information) confirm all these are crucial.

2.2. Characterization of Catalysts

The scanning transmission electron microscopy (STEM) image of the $Co_{0.2}Pd_{1.8}$-TiO_2 is shown in **Figure 2A**. Small Pd nanoparticles with a mean diameter of 4 nm are uniformly dispersed on the surface of $Co_{0.2}Pd_{1.8}$-TiO_2 after analyzing > 80 Pd nanoparticles. The aberration-corrected STEM in Figure 2B shows the lattice spacings of 2.37 and 2.15 Å, corresponding to {001} facet of anatase TiO_2 and {110} facet of PdO. Typically, the intensity of the atomic fringes in an aberration-corrected HRTEM micrograph correlates with the atomic mass.[18] The bright points in atomic fringes were marked with grey dotted circles and analyzed using the line scanning. As shown in Figure 2C,D, the difference in intensities observed in the line scanning results of 1 # and 2 # marked in Figure 2B is likely due to the higher atomic number of Co (27) compared to Ti (22).

To further evidence the atomic dispersion of Co species, X-ray absorption spectroscopy (XAS) was carried out. As shown in Figure 2E, the X-ray absorption near-edge structure (XANES) spectra of Co K-edge show that the K-edge absorption energy of $Co_{0.2}Pd_{1.8}$-TiO_2 locates between that of CoO and Co_3O_4, suggesting the state of Co species is between +2 and +3. The K^3-weighted FT extended X-ray absorption fine structure (EXAFS) spectra are shown in Figure 2F. The $Co_{0.2}Pd_{1.8}$-TiO_2 presents only one strong peak at 1.47 Å corresponding to Co–O peak, and there is no clear peak in the region of 2–3 Å that corresponds to the Co-Co peak of either Co foil, CoO, or Co_3O_4. These results confirm that the Co species are atomically dispersed and coordinated by O atoms, consistent with the HADDF-STEM image.[19–21]

The high angle annular dark-field (HAADF) image of $Co_{0.2}Pd_{1.8}$-TiO_2 is shown in Figure S11A (Supporting Information), and the region in the red dotted rectangle was analysed by energy dispersive X-ray (EDX). The Co, Pd, Ti, and O EDX maps are shown in Figure S11B (Supporting Information), confirming the uniform distribution of the four elements, while the Co and Pd elements exist independently with little correlation. The X-ray diffraction (XRD) patterns (Figure S12, Supporting Information) show that all peaks can be indexed to TiO_2 (JCPDS NO. 21–1272). There are no peaks assigned to Co or Pd species, indicating that the photodeposition of Co and then Pd does not alter the crystal phase of TiO_2, and the loaded metals are evenly dispersed.[22] The UV–vis spectra (Figure S13, Supporting Information) of Co_xPd_y-TiO_2 catalysts present the characteristic absorption bands with an onset edge at 400–410 nm and a bandgap of 3.1–3.0 eV, corresponding to the bandgap transition of TiO_2.[23] Additionally, no activity for methane conversion over $Co_{0.2}Pd_{1.8}$-TiO_2 can be observed under the irradiation by visible Xenon lamp (>450 nm) (Figure S14, Supporting Information). All these suggest that TiO_2 was excited by UV irradiation and driven the catalytic CH_4 conversion process. The loading of Co and Pd has no obvious effect on the light absorption of the photocatalysts. Thermogravimetric analysis (TGA) (Figure S15, Supporting Information) of photocatalyst samples indicates that the catalyst has good thermal stability at the reaction room temperature. When being excited by

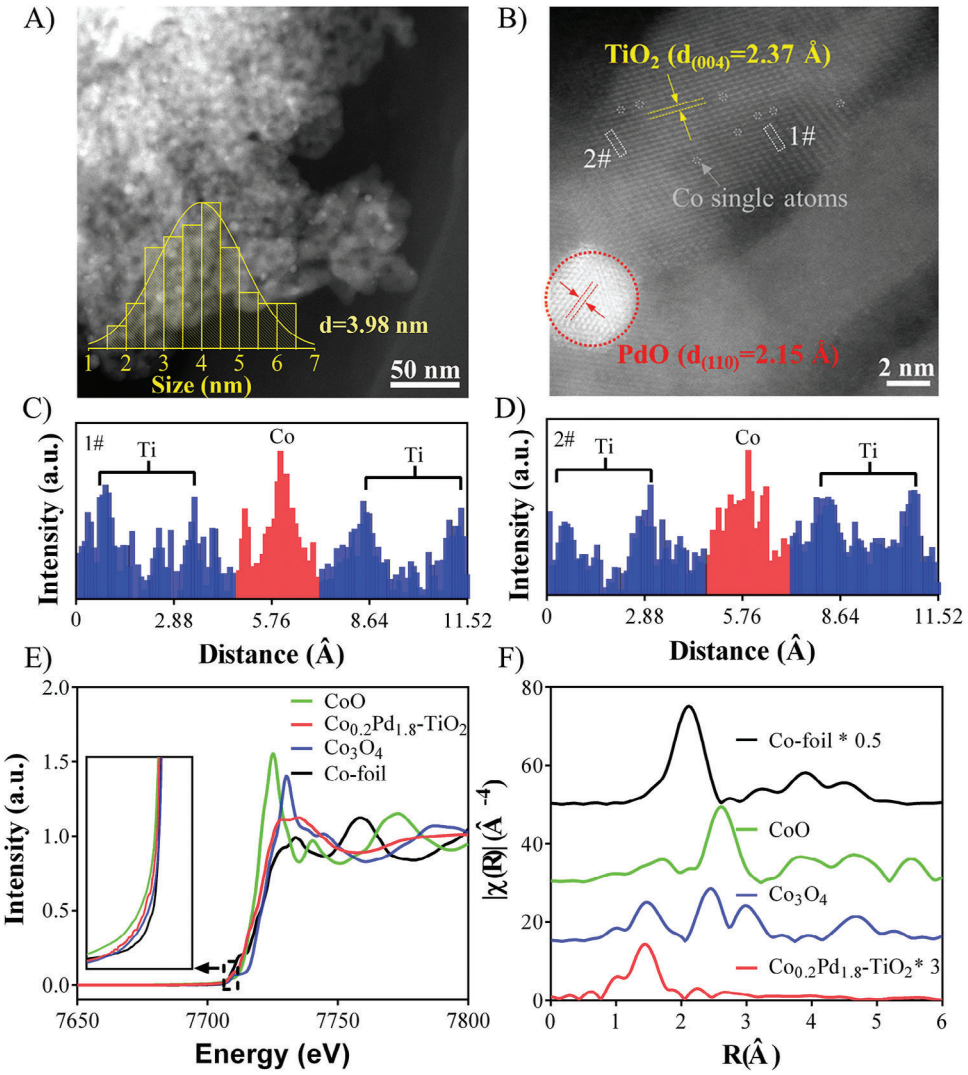

Figure 2. Physical characterizations of catalysts. A) STEM image of $Co_{0.2}Pd_{1.8}$-TiO_2, the inset is the particle size distribution of Pd. B) HADDF-STEM image of $Co_{0.2}Pd_{1.8}$-TiO_2, where Co single atoms are marked by grey dotted boxes. C,D) Line scan results of the 1 #, 2 # marked in (B). E) Co K-edge XANES spectra of $Co_{0.2}Pd_{1.8}$-TiO2. The inset enlarges the dotted-box area. F) K^3-weighted FT EXAFS spectrum of $Co_{0.2}Pd_{1.8}$-TiO_2, in which Co_3O_4, CoO, and Co foil are used as references.

light, the activity of the photocatalyst is closely related to its charge separation ability.

X-ray photoelectron spectroscopy (XPS) characterization was conducted with light irradiation in a vacuum chamber to ex situ investigate the charges separation and transfer in $Co_{0.2}Pd_{1.8}$-TiO_2. The Pd 3d XPS spectra are shown in **Figure** 3A and Table S3 (Supporting Information). Under both dark and light-irradiated conditions, the Pd $3d_{3/2}$ spectra could be ascribed into three species corresponding to Pd^0, Pd^{2+}, and Pd^{4+}, which are located at 340.09, 341.56, and 342.76 eV respectively.[24,25] The results indicate that during the photodeposition process, Pd particles first form, and then a portion of Pd is oxidized to higher valence states (Pd^{2+} and Pd^{4+}).[26] Under light irradiation, the ratio of Pd^0 decreases from 55.77% to 44.90% while the ratios of Pd^{2+} and Pd^{4+} increase from 38.06% and 6.17% to 42.61% and 12.49% respectively. These results indicate that the Pd species could capture the holes, thus presenting the oxidizing capacity.

On the other hand, the XPS peaks of Co 2p are difficult to be detected due to its very low loading amount (0.2 wt%) in $Co_{0.2}Pd_{1.8}$-TiO_2. Thus, a sample loaded with 2.0% wt. of Co species was prepared by the same procedure and used to identify the function of Co species in the charge transfer.[27] Figure 3B and Table S4 (Supporting Information) show that the main peaks of Co^{x+} $2p_{1/2}$, Co $2p_{1/2}$, Co^{x+} $2p_{3/2}$, and Co $2p_{3/2}$ are located at 796.8, 793.7, 781.3, and 778.5 eV, respectively, with their corresponding satellite peaks positioned at 803.5, 800.4, 787.5, and 784.6 eV, respectively.[28] The ratio of Co^0 under light irradiation increases from 12.01% to 21.29% while the ratio of Co^{x+} decreases from 87.99% to 78.71%. These results show that the electrons could be easily transferred to Co^{x+} under light irradiation. To sum up, the Co species and Pd species both play decisive and explicit roles in promoting electrons and holes separation, respectively. The increased current density of *I-T* curves further confirms the promoted charge separation by Co and Pd (Figure S16,

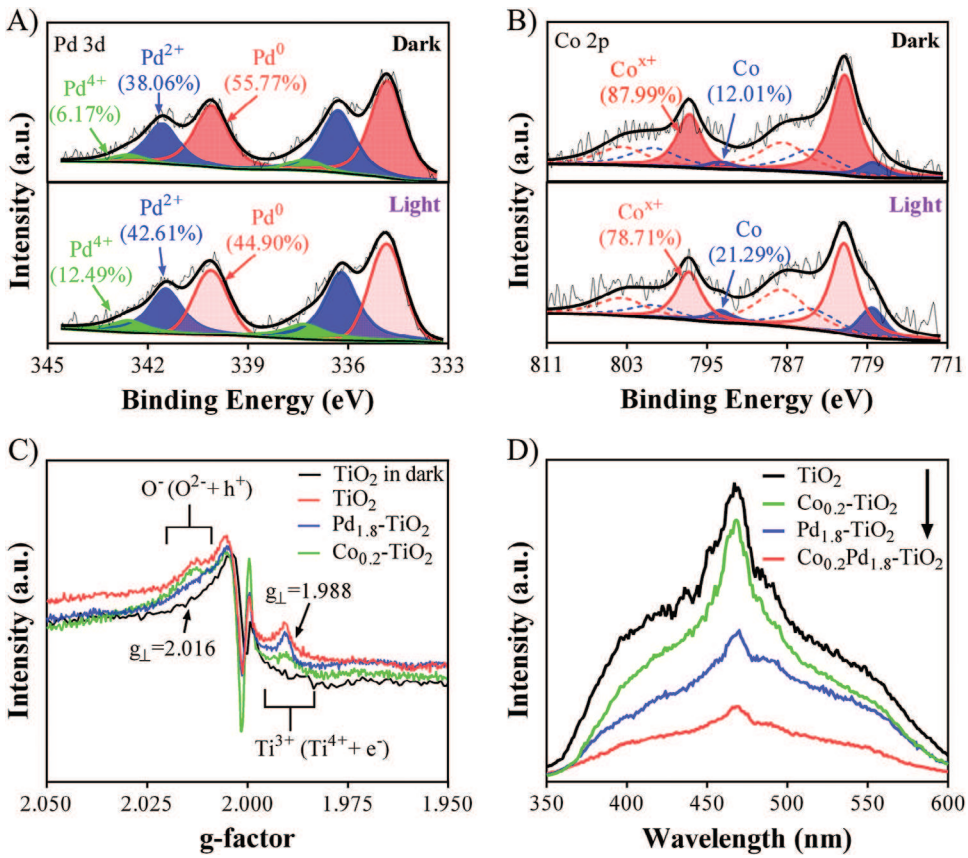

Figure 3. Photophysical characterizations of catalysts. A) XPS spectra of Pd 3d of $Co_{0.2}Pd_{1.8}$-TiO_2 in the dark and under light irradiation. B) XPS spectra of Co 2p of $Co_{2.0}Pd_{1.8}$-TiO_2 in the dark and under light irradiation. (The black bold lines serve to illustrate the baselines and the fitted curves, while the black fine lines denote the raw data traces. In inset (B), the dashed lines indicate the satellite peak curves attributed to the Co element). C) EPR spectra of samples in the dark and under light irradiation. D) PL spectra of TiO_2, $Co_{0.2}$-TiO_2, $Pd_{1.8}$-TiO_2, and $Co_{0.2}Pd_{1.8}$-TiO_2.

Supporting Information). Next, the in situ electron paramagnetic resonance (EPR) was carried out to further clarify the direction of the charge transfer. Under 365 nm LED illumination, the signal of Ti^{3+} sites at $g_{\perp}$ = 1.988 and O^- sites at $g_{\perp}$ = 2.016 can be observed, while they are not noticeable under the dark condition (Figure 3C; Figures S17–S19, Supporting Information).[29–31] There is only Ti^{3+} signal that can be observed in $Pd_{1.8}$-TiO_2 under light irradiation, while the O^- signal in $Pd_{1.8}$-TiO_2 has disappeared. It demonstrates that the Pd species can trap the holes to reduce the formation of O^- sites (Figure S17, Supporting Information). Meanwhile, the Ti^{3+} signal of $Co_{0.2}$-TiO_2 is greatly weakened under light irradiation (Figure S18, Supporting Information), indicating that the Co atoms capture electrons and reduce the generation of Ti^{3+}. For $Co_{0.2}Pd_{1.8}$-TiO_2 sample, the signals of Ti^{3+} and O^- are simultaneously weakened under light irradiation (Figure S19, Supporting Information). This suggests the synergistic effect of PdO_L and Co single atoms, which can capture holes and electrons, respectively, and without interfering with each other. In addition, the intensities of photoluminescence (PL) signals are in the order of TiO_2> $Co_{0.2}$-TiO_2> $Pd_{1.8}$-TiO_2> $Co_{0.2}Pd_{1.8}$-TiO_2, ascribed to the weakening of photogenerated charge recombination (Figure 3D). The EPR and PL results unambiguously indicate that Co single atoms and PdO_L capture electrons and holes, respectively, thus improving the charge separation.

2.3. Mechanistic Insight into the Chemical Cycle Reaction Pathways

The effect of introduced Co single atoms on the state of Pd species in the as-prepared catalyst was investigated by comparing the XPS spectra of Pd 3d for $Pd_{1.8}$-TiO_2 and $Co_{0.2}Pd_{1.8}$-TiO_2 (**Figure 4A**). The ratio of Pd^0 in $Pd_{1.8}$-TiO_2 (76.31%) is larger than that in $Co_{0.2}Pd_{1.8}$-TiO_2 (55.77%), while the $Co_{0.2}Pd_{1.8}$-TiO_2 has a larger concentration of Pd^{2+} (38.06%) than that in $Pd_{1.8}$-TiO_2 (20.29%) (Table S5, Supporting Information), suggesting Co single atoms can increase the amount of the high valence of palladium in the prepared photocatalysts.

H_2-TPR experiments of $Pd_{1.8}$-TiO_2 and $Co_{0.2}Pd_{1.8}$-TiO_2 were conducted as a supplement. As shown in Figure S20 (Supporting Information), a broad reduction feature ranging between 70 and 210 °C can be attributed to the consumption of H_2 during the reduction of PdO species.[32] The H_2 consumption of $Co_{0.2}Pd_{1.8}$-TiO_2 (with an integral area of 639) is greater than that of $Pd_{1.8}$-TiO_2 (with an integral area of 493), indicating that the PdO

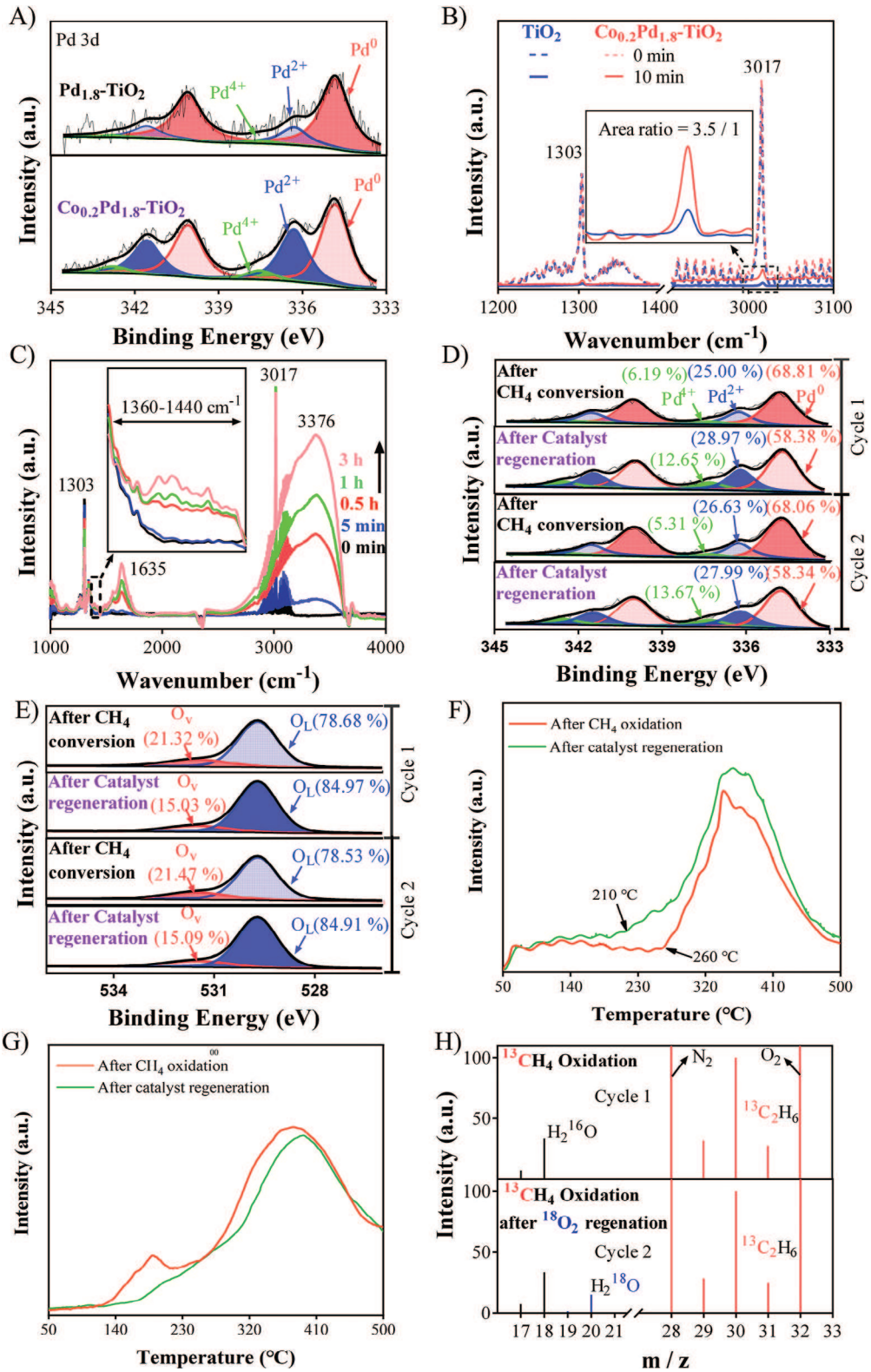

Figure 4. Analysis of reaction mechanism. A) XPS spectra of Pd 3d for $Pd_{1.8}$-TiO_2 and $Co_{0.2}Pd_{1.8}$-TiO_2 under dark conditions. B) In situ DRIFT spectra of CH_4 desorption on $Co_{0.2}Pd_{1.8}$-TiO_2 and TiO_2, the inset is the ratio of adsorbed CH_4 (3016 cm^{-1}) on $Co_{0.2}Pd_{1.8}$-TiO_2 and TiO_2. C) In situ DRIFT spectra of CH_4 conversion over $Co_{0.2}Pd_{1.8}$-TiO_2, the inset shows the peak of C_2H_6. D) Pd 3d XPS spectra, E) O 1s XPS spetra, F) H_2-TPR, and G) O_2-TPO of $Co_{0.2}Pd_{1.8}$-TiO_2 after the CH_4 conversion and catalyst regeneration steps during the chemical cycle process. H) Mass spectra of the isotope labeling experiments.

content in $Co_{0.2}Pd_{1.8}$-TiO_2 is higher than that in $Pd_{1.8}$-TiO_2. These results are consistent with the XPS results shown in Figure 4A. Furthermore, the reduction feature observed between 260 and 500 °C can be attributed to the consumption of H_2 during the reduction of lattice oxygen of the TiO_2.[33] Notably, $Co_{0.2}Pd_{1.8}$-TiO_2 and $Pd_{1.8}$-TiO_2 exhibit similar H_2 consumption in this range, with the integral area of 3102 and 3065, respectively. As confirmed above, the state of Co species is between +2 and +3; combining with the above XPS result, it could be inferred that Co species could in part act as electron accept mediators to promote the formation of PdO_L during the catalyst preparation.[14]

Following the enhanced charge separation, the next step for CH_4 conversion is its adsorption on the surface of photocatalysts, which was monitored by diffuse reflectance infrared Fourier transform (DRIFT). As shown in Figure 4B, the tetrahedral symmetry of the CH_4 molecule leads to the degenerate overtone and combined vibration states involved in successive polyads which are split into sub-levels. The DRIFT results obtained for $Co_{0.2}Pd_{1.8}$-TiO_2 and TiO_2 exhibit multiple IR adsorption peaks of CH_4 in the ranges of 1200-1040, 2900–3100 cm^{-1} in the dark.[34] After purging by Ar gas for 10 min, the physically adsorbed CH_4 on the TiO_2 could be greatly removed. In contrast, the CH_4 adsorbed on the $Co_{0.2}Pd_{1.8}$-TiO_2 has considerable residual presence. The area ratio of DRIFT peak at 3017 cm^{-1} on $Co_{0.2}Pd_{1.8}$-TiO_2 to that on TiO_2 is 3.5 (insert of Figure 4B), which implies that CH_4 molecules prefer to adsorb on the $Co_{0.2}Pd_{1.8}$-TiO_2 rather than bare TiO_2.[34] The enhanced CH_4 adsorption capacity of $Co_{0.2}Pd_{1.8}$-TiO_2 could benefit the mass transfer between CH_4 molecules and solid catalyst to promote catalytic activity, especially in a flow reactor.[35]

To get a clear understanding of the chemical cycle reaction pathway over $Co_{0.2}Pd_{1.8}$-TiO_2, especially to verify the formation of the products, the DRIFT spectra were recorded under light irradiation. As shown in Figure 4C, new peaks appear at 3376 and 1635 cm^{-1}, and their intensity increases with light illumination. These new bands could be attributed to the stretching vibration and bending vibration of the O−H bond in H_2O.[36] It is worth noting that the peaks observed at 2330 and 2360 cm^{-1} are attributed to the stretching vibration of the C-O bond in the adsorbed CO_2 species (Figure S21, Supporting Information). It is apparent that the intensity of these peaks is weaker after 1 hour of reaction and remains unchanged after 3 hours of reaction. This indicates that no significant amount of CO_2 is produced, which is consistent with the results of products analysis in the CH_4 conversion step. Meanwhile, the CH_4 peaks at 1303 and 3017 cm^{-1} decrease under light irradiation. Notably, a new peak ≈1360–1440 cm^{-1} is observed and increases with irradiation time (Insert of Figure 4C), which is assigned to C_2H_6.[37]

The results reveal that C_2H_6 and H_2O are formed during the CH_4 chemical cycle reaction, consistent with the Equation (1). As mentioned earlier, the O_L of PdO_L is consumed in step 1 (CH_4 conversion) and then compensated in step 2 (catalyst regeneration) during the chemical cycle process. Herein, the Pd 3d XPS spectra of $Co_{0.2}Pd_{1.8}$-TiO_2 were used to monitor the change of the oxidation states of Pd in the chemical cycle. The Pd 3d XPS spectra of $Co_{0.2}Pd_{1.8}$-TiO_2 were recorded after CH_4 conversion for 1 h and then after regeneration for 5 min, respectively. As shown in Figure 4D and Table S6 (Supporting Information), the Pd^0 content of $Co_{0.2}Pd_{1.8}$-TiO_2 after CH_4 conversion reaction for 1 h is 68.81%, which is higher than that of the fresh sample shown in Table S5 (Supporting Information) (55.77%). Then, the dry air was pumped into the reactor under light irradiation. The Pd^0 content decreased to 58.38%. After that, CH_4 was pumped and reacted again. The Pd^0 content increased to 68.06%. Repeating the operation of pumping dry air into the reactor under light irradiation, the Pd^0 content decreased to 58.34%. Additionally, the C1s XPS spectra of $Co_{0.2}Pd_{1.8}$-TiO_2 were also recorded. As shown in Figure S22 (Supporting Information), the C1s spectra exhibit signals attributed to C-C and C═O at 284.6 and 288.5 eV respectively,[38,39] which were introduced due to carbon contamination. It can be observed that after two cycles involving both the methane conversion process and the catalyst regeneration process, the C1s XPS results remain unchanged. These results indicate the absence of carbon deposition during the chemical cycle, thereby maintaining the long-term stability. The O1s XPS spectra of $Co_{0.2}Pd_{1.8}$-TiO_2 were also recorded. Figure 4E shows two peaks at 531.5 and 529.7 eV, which are assigned to adsorbed hydroxyl at an oxygen vacancy and lattice oxygen (O_L) signals, respectively.[40–42] When lattice oxygen is consumed during reactions, creating oxygen vacancies, these vacancies promote dissociative adsorption of water, which consequently leads to the emergence of hydroxyl signals (at 531.5 eV) in X-ray photoelectron spectroscopy (XPS) results. An increased generation of oxygen vacancies corresponds to a heightened production of hydroxyl signals, providing a direct correlation between the abundance of oxygen vacancies and the intensity of hydroxyl-related signals. Hence, in this work, we denote this signal as "O_v" to present a more intuitive depiction of the changes in the number of oxygen vacancies throughout the reaction progression.

The O_v content is 21.32% after the first step in the chemical cycle (cycle 1), and decreases to 15.03% after the second step in the chemical cycle (cycle 1), implying that the O_v are refilled. Repeating the chemical cycle operation again, te O_v content increases to 21.47% in the first step and decreases to 15.09% in the second step. All these changes well coincide with the Pd valence changes in the two steps of chemical cycle, which verify that the O_L of PdO_L is consumed during the CH_4 conversion, leading to the formation of O_v, and the regeneration induces oxygen to fill the O_v. Oxygen vacancies on the surface of TiO_2 are closely related to the presence of Ti^{3+} on the TiO_2 surface.[43] As shown in Figure S23 (Supporting Information), the Ti 2p XPS spectra confirm that the oxygen vacancies in TiO_2 remain largely unchanged. Therefore, during the chemical cycling process, the O_L of PdO_L is primarily consumed, leading to the formation of O_V (Figure 4E). In addition to XPS and EPR, H_2 temperature-programed reduction (H_2-TPR) and O_2 temperature-programmed oxidation (TPO) were conducted using a Micromeritics AutoChem II analyzer to further corroborate the changes in Pd states. The H_2-TPR profiles of $Co_{0.2}Pd_{1.8}$-TiO_2 during the two steps of the chemical cycle process are presented in Figure 4F. A broad reduction feature ranging from 70 to 210 °C is attributed to the H_2 consumption during the reduction of PdO species.[32] The H_2 consumption of the regenerated catalyst is higher than that of the used catalyst, indicating the presence of larger amounts of O_L of PdO_L species in the regenerated catalyst, which is consistent with the results of Figure 4D. The reduction feature ranging from 260 to 500 °C is attributed to the consumption of H_2 during the reduction of lattice oxygen of the TiO_2.[33] The regenerated catalyst consumes

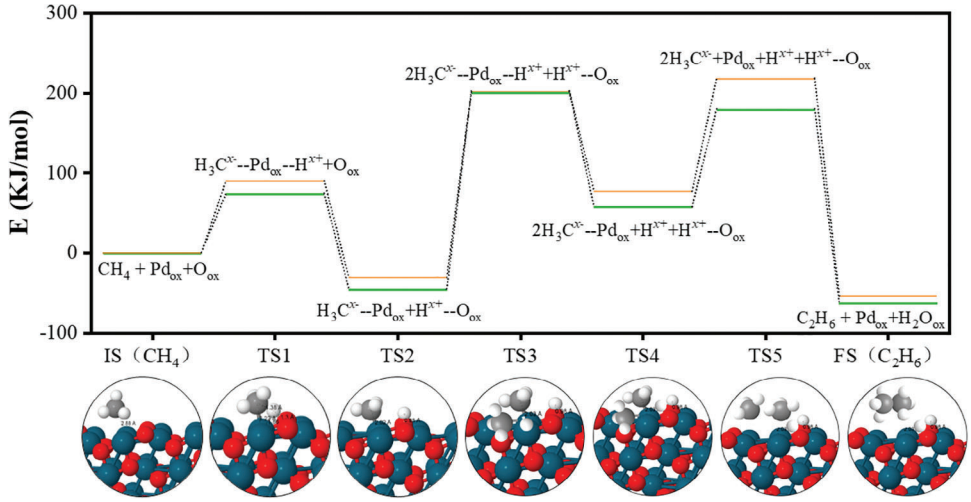

Figure 5. DFT simulations of CH_4 conversion. Energy diagrams for conversion of adsorbed CH_4 to C_2H_6 on PdO. (Orange lines represent the neutral system, green lines represent the positively charged system).

more H_2 than the used catalyst, indicating that lattice O of TiO_2 also participates in the oxidation reaction, which coincides with the change in O states (Figure 4E). It is noteworthy that the regenerated catalyst exhibits much better redox ability, reflected by the shift of the starting position of reduction peaks to lower temperatures. Correspondingly, the O_2-TPO results (Figure 4G) also show two regions and confirm that the used catalyst consumes more O_2. The region ranging from 140–230 °C is attributed to supplementing O_L (O_L of PdO_L species and TiO_2), while the region of 230–500 °C is attributed the oxidation of metallic Pd.[44–46] Thus, both H_2-TPR and O_2-TPO are in good agreement, supporting Pd valence change during the chemical cycle process. After the C-H bond is cleaved by O_L, the resulting intermediate $\cdot CH_3$ attached to PdO_L could form a more stable transition state (CH_3–Pd–OH), next forming C_2H_6 instead of the continuous dehydrogenation.[47] Due to the very lean oxygen environment only provided by O_L, overoxidation is avoided in the catalytic process, leading to high selectivity to ethane. In parallel, Co can clean the surface of the photocatalyst by promoting the reduction reaction between proton and ·OH radical to water. After the catalyst is regenerated in the dry air, the Pd^0 content of $Co_{0.2}Pd_{1.8}$-TiO_2 (58.38% – 58.34%) drops back to the same level as the as-prepared $Co_{0.2}Pd_{1.8}$-TiO_2 (ca. 55.77%).[14] Then the catalytic activity is recovered after the regeneration step and could be well-maintained up to 43-cycles run (Figure 1C). To solidly confirm that the O_L is consumed through participating in the oxidation of CH_4 and is induced again during the catalyst re-oxidation process, isotopic labeling experiments were carried out in a batch reactor. In the first cycle of the chemical cycle process, the as-prepared catalyst reacted with $^{13}CH_4$ under light irradiation. As shown in the top panel of Figure 4H, the m/z = 28, 29, 30, 31, and 32 are assigned to $^{13}C_2H_6$ and it fragments.[12] The signals at m/z = 28 and 32 are interfered by the signals of residual N_2 and O_2, primarily due to contamination that occurs during the extraction process of the product from the reactor and its subsequent transfer into the gas chromatography-mass spectrometry (GC-MS) instrumentation for detection purposes. This particular category of interference can be predominantly ascribed to the constraints limitations of the detection equipment. $^{13}C_2H_3^+$, $^{13}C_2H_4^+$, and $^{13}C_2H_5^+$ ions (m/z = 29, 30 and 31) that are fragments of C_2H_6, prove that CH_4 is the carbon source for C_2H_6 formation. Meanwhile, the $H_2{}^{16}O$ MS signal is observed mainly at m/z = 18. In the second cycle of the chemical cycle process, the $^{18}O_2$ was filled first in the reactor to regenerate the catalyst. After that the $^{13}CH_4$ was pumped in. As shown in the bottom panel of Figure 4H, the $H_2{}^{18}O$ (m/z = 20) MS signals are observed besides $H_2{}^{16}O$ during CH_4 conversion. This proves that O_L acts as an oxidant and is in part consumed during CH_4 conversion reaction, leaving O_v. When introducing $^{18}O_2$ in the regeneration step, O_v can be replenished by ^{18}O, resulting into the $H_2{}^{18}O$ signal during the subsequent CH_4 conversion reaction. All these results further confirm a complete chemical cycle used for photocatalytic methane oxidation.

In addition, a DFT study was conducted to investigate the process of conversion of adsorbed CH_4 to C_2H_6. The obtained results are presented in **Figure 5** and Table S7 (Supporting Information), which displays the structures of the reactants (IS), transition state (TS), and products (FS), along with the energy changes shown as orange and green lines, corresponding to the neutral and positively charged systems, respectively. The results reveal that the neutral system requires 89.4 kJ mol^{-1} to overcome the activation barrier for the first adsorbed CH_4 to break a C-H bond, leading to the formation of an adsorbed CH_3 species and an adsorbed H. However, the positively charged system, where PdO has captured a photogenerated hole, exhibits a lower activation barrier of 73.58 kJ mol^{-1}. Moreover, the TS2 product in the charged system is more stable (−45.94 kJ mol^{-1}) than in the neutral system (−30.97 kJ mol^{-1}). The second adsorbed CH_4 (TS3) requires 200.28 kJ mol^{-1} to overcome the activation barrier in the positively charged system, which is slightly lower than that in the neutral system (201.66 kJ mol^{-1}). The TS4 product in the charged system is also more stable (56.88 kJ mol^{-1}) than in the neutral system (76.25 kJ mol^{-1}). In the TS4 process, 179.03 kJ mol^{-1} is required in the positively charged system, which is lower than that in the neutral system (217.33 kJ mol^{-1}). In addition, the FS product in the charged system is more stable (−63.25 kJ mol^{-1})

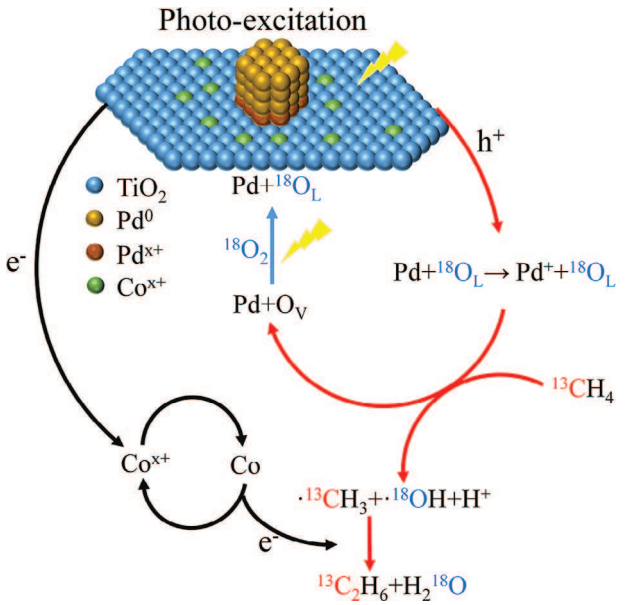

Scheme 1. Proposed mechanism of synthesis of ethane from methane by the chemical cycle process, herein O_L: lattice oxygen, O_v: oxygen vacancy.

compared to the neutral system (−54.4 kJ mol^{-1}). The lower activation energy can be attributed to the shorter distance between CH_4 and PdO in the positively charged system (C-Pd interatomic distance of 2.65 Å) than in the neutral system (C-Pd interatomic distance of 2.88 Å) due to the presence of holes causing stronger attraction of CH_4 to the surface. Table S8 (Supporting Information) shows that the H^{x+} atom involved in C-H bond breaking becomes more positive moving from the reactant (+0.141) to the product (+0.415), which can be interpreted as adsorbed H^+ or formation of surface ·OH. The surface O_{ox} atom involved in H adsorption becomes more negative in the conversion from the reactants (−0.497) to the products (−0.572), as the hole moves from O_{ox} to H_{ox}. The PdO slab overall becomes less positive in the conversion from the reactants (+0.826) to the products (+0.583), as the hole partially moves to H adsorbed on O. Based on these results, dissociation of the C–H bond of adsorbed CH_4 is facilitated thanks to the presence of photogenerated holes on PdO, leading to the formation of C_2H_6.

Sed on the above discussions, the reaction pathway is proposed in **Scheme 1**. In this chemical cycle process, the CH_4 conversion step and the catalyst regeneration step are alternately operated to form a cycle. First, $Co_{0.2}Pd_{1.8}$-TiO_2 is excited by the light irradiation to produce electrons and holes, which are separately attracted by Co single atoms and PdO_L, respectively. The adsorbed CH_4 is cleaved over PdO_L to form·CH_3, H^+, and ·OH, in which the O_L of PdO_L is consumed and the partially reduced Pd species are produced (denoted Pd in the Scheme). The generated ·CH_3 radicals spontaneously couple to form C_2H_6, which desorbs from the catalyst surface and flows out of the reactor. In parallel, the electrons trapped by Co single atoms participate in the reduction reaction of H^+ and ·OH to form H_2O. With the O_L of PdO_L consumed over time, the activity of $Co_{0.2}Pd_{1.8}$-TiO_2 gradually decreases. Then $Co_{0.2}Pd_{1.8}$-TiO_2 catalyst is regenerated by oxidization of the partially reduced Pd species by air to form PdO_L. The regenerated photocatalyst can be successfully used in the next cycles, leading to high selectivity and stability in the 43 cycles.

3. Conclusion

To summarise, coupling the chemical cycle process with a flow reactor using the optimized $Co_{0.2}Pd_{1.8}$-TiO_2 catalyst has resulted in continuous, efficient, and selective CH_4 conversion under mild and O_2-free conditions. The PdO_L nanoclusters and Co single atoms were loaded on TiO_2 with distinct and complementary functions. The $Co_{0.2}Pd_{1.8}$-TiO_2 catalyst thus achieves CH_4 conversion to C_2H_6 with the yield of 74 μmol·g^{-1}·h^{-1} (or 3.7 μmol·h^{-1}) and a selectivity of near 100% operated at room temperature. The function of PdO_L species is proved to attract photogenerated holes and to directly cleave the C-H bond. In the meantime, the O_L of PdO_L is consumed to form ·CH_3 and ·OH by oxidation of CH_4. The recombination of ·CH_3 preferentially produces C_2H_6. In parallel, photogenerated electrons are attracted by Co single atoms and are used to reduce ·OH and H^+ to form H_2O. In the subsequent step of the catalyst regeneration, the consumed O_L of PdO_L is replenished by air under light irradiation, leading to a high stability over a 43 cycles test. Overall, this work not only proposes a novel strategy that employs a chemical cycle to modulate reaction intermediate and products, leading to efficient and selective conversion of CH_4 to value-added products, but also opens a new avenue to construct advanced catalysts with multifunction sites to overcome the issue of charge recombination in photocatalysis. In addition, this process avoids mixing the flammable gas CH_4 with O_2 for chemicals production, improving the process safety of this important chemical reaction.

4. Experimental Section

Chemicals and Materials: All the aqueous solutions were prepared using deionized water without further purification. Titanium dioxide (TiO_2, 60 nm, anatase, 99.8%, Alfa Aesar), ethylene glycol (EG, 99.5, Greagent), hexaamminecobalt (III) chloride ($[Co(NH_3)_6]Cl_3$, 99%, Macklin), potassium tetrachloropalladate(II) (K_2PdCl_4, 99%, Adamas), ammonium hydroxide solution (NH_4OH, 29%, Adamas), and hydrochloric Acid (HCl, 37%, Adamas) were separately applied in the experimental studies.

Preparation of TiO_2: Anatase TiO_2 (1 g, 60 nm) and 30 mL EG were mixed together and then stirred rapidly for 1 h. The products were collected after centrifugation and further washed with deionized water three times, which was denoted as TiO_2.

Preparation of Co_x-TiO_2: TiO_2 (0.25 g) was first suspended in the aqueous methanol solution (10 vol.%), where different amounts of $[Co(NH_3)_6]Cl_3$ were then added. After purging with ultrapure Ar for 30 min in the dark, the suspensions were sealed and irradiated. After the 4 h irradiation, the products were collected following centrifugation and further washing with DI water. After drying, the obtained samples were used for characterizations and catalysis tests. The final products were named as Co_x-TiO_2, where x represented the mass percentage of Co to TiO_2 substrates. The actual Co loadings were then measured by ICP-AES, and the values of x were 0.12, 0.15, 0.2, and 0.24, respectively.

Preparation of $Pd_{1.8}$-TiO_2: TiO_2 (0.25 g) was first suspended in the aqueous methanol solution (10 vol.%), where certain amounts of K_2PdCl_4 were then added. After purging with ultrapure Ar for 30 min in the dark, the suspensions were sealed and irradiated. After the 4 h irradiation, the products were collected following centrifugation and further washing with DI water. After drying, the obtained samples were used for characterizations and catalysis tests. The final products were named as $Pd_{1.8}$-TiO_2, where 1.8 represented the 1.8% wt. percentage of Pd to TiO_2 substrates.

Preparation of Co_xPd_y-TiO_2: Co_x-TiO_2 (0.25 g) was first suspended in the aqueous methanol solution (10 vol.%), where certain amounts of K_2PdCl_4 were then added. After purging with ultrapure Ar for 30 min in the dark, the suspensions were sealed and irradiated. After the 4 h irradiation, the products were collected following centrifugation and further washing with DI water. After drying, the obtained samples were used for characterizations and catalysis tests. The final products were denoted as Co_xPd_y-TiO_2, where x and y represented the mass percentage of Co and Pd relative to TiO_2 substrate, respectively. The actual Co and Pd loadings were then measured by ICP-AES (x = 0, 0.12, 0.15, 0.2, 0.24, and y = 0, 1.1, 1.4, 1.8, 2.1).

Characterisation: TEM images were acquired via a field-emission TEM system (FEI Talos F200X). The FEI Talos F200X equipped with an Energy-dispersive X-ray (EDX) Detector was used to conduct element analysis of the samples. STEM images were obtained with a spherical aberration corrected TEM system (Titan Cubed Themis G2 300). XRD patterns were obtained on a Bruker D8 Advance fitted with a solid-state X' Celerator detector (2.2 kw) using Cu Kα radiation from 5 to 80°. The scan speed and step size of the measurements were 10.0° min^{-1} and 0.02° in 2θ, respectively. The UV–vis absorption spectra (UV–vis abs) of the samples were acquired using a Shimadzu UV 3600 plus spectrophotometer with $BaSO_4$ as the reference. XPS analysis was investigated using a Thermo ESCALAB 250Xi instrument equipped with an Al Kα radiation source. The measurements were conducted in a vacuum chamber, with data collection performed both before light irradiation and after irradiation for 20 minutes. A 365 nm LED was employed as the excitation source. The normal XPS was performed on an Ulvac-Phi PHI5000 VersaProbeIII system with an Al Kα source. All XPS spectra were corrected using C 1s line at 284.6 eV. The contents of various elements were measured by an ICP-MS (Agilent 7900). Time resolved fluorescence spectra were collected on an FLSP920 spectrofluorometer with the excitation wavelength of 310 nm. The electron paramagnetic resonance (EPR) measurements were carried out on a Bruker E500-9.5/12 spectrometer operating at the X-band frequency at room temperature. 30 mg powder sample was weighed and a 365 nm LED was applied as the irradiation source. The XAFS spectra were recorded at room temperature using a 4-channel silicon drift detector (SDD) Bruker 5040. Co K-edge extended X-ray absorption fine structure (EXAFS) spectra were recorded in fluorescence mode. The spectra were processed and analysed by the software code Athena.

In Situ Diffuse Reflectance Infrared Fourier Transform Spectroscopy (DRIFT) Measurements: The DRIFT spectra were collected on a Nicolet IS50 spectrometer equipped with a mercury cadmium telluride (MCT) detector. All loaded samples were pretreated at 80 °C for 12 hours and then cooled down to room temperature. 5 mg of sample was loaded into the tablet machine under 1 MPa pressure, and the obtained wafer was mounted into a quartz IR cell-reactor with a CaF_2 window. After Ar purge for 30 min, the background spectra were collected on the pretreated samples. CH_4/Ar (flow rate = 50 mL·min^{-1}) was introduced for 30 min to reach adsorption saturation. Desorption spectra were obtained after Ar purges for 0, 1, 3, 5, and 10 minutes. The CH_4 conversion reaction was performed after an Ar purge for 3 min with various reaction times of 5, 30, 60, and 180 minutes. Then the IR spectra of the CH_4 desorption and oxidation reaction were collected during the processes described above.

Photocatalytic Activities for CH_4 Conversion: Sample powder (50 mg) was suspended in 50 mL of water with magnetic stirring in a beaker. Then, the suspension was filtered through a nylon membrane (diameter 35 mm) to produce a uniform film. After drying at 60 °C for 12 hours, the film was placed on the copper grid of a flow reactor equipped with a temperature probe to monitor the reaction temperature. For each experiment, the system was purged with Ar (50 mL·min^{-1}) for 30 minutes. Subsequently, the reactor was irradiated by a LED light source (365 nm Beijing Perfect Light, PLS-LED 100B) for 1 hour with a CH_4 flow rate of 50 ml min^{-1}. Then the dry air was pumped into the system and irradiated for 5 minutes to regenerate the catalyst. Finally, the outlet gases were detected by an SP-3420A GC equipped with a thermal conductivity detector (TCD) and a flame ionization detector (FID).

Isotope Labelling Experiment: In the first step of the chemical cycle process, the as-prepared sample film was placed in a batch reactor and degassed using a vacuum pump to remove air. The reactor was then filled with $^{13}CH_4$. The reaction was carried out at 25 °C under light irradiation for 1 hour. The products were collected by a gas collecting bag. After that, the reactor was degassed and refilled with $^{18}O_2$. Then the reaction of catalyst regeneration was carried out at 25 °C under light irradiation for 5 min. After that, the reactor was degassed and refilled with $^{13}CH_4$ again. The CH_4 conversion was carried out at 25 °C under light irradiation for 1 hour. The products were collected in another gas collecting bag. Then the collected products were measured by GC-MS (QP2010Plus, Shimadzu Co., Ltd) equipped with the Rtx-Wax column.

Calculation of Selectivity: The selectivity for C_2H_6 was calculated as below:

$$C_2H_6 \text{ selectivity} = \frac{2 \times n\,(C_2H_6)}{2 \times n\,(C_xH_y) + n\,(CO_2) + n\,(CO)} \quad (4)$$

C_xH_y represents all C_2 hydrocarbons that can be detected.
The apparent quantum yield (AQY) was calculated by:

$$\text{AQY} = \frac{N_e}{N_P} \times 100\% = \frac{10^9 \times \upsilon \times N_A \times K \times h \times c}{I \times A \times \lambda} \times 100\% \quad (5)$$

where υ is the conversion rate of CH_4 (mol/s), N_A is the Avogadro constant, K is number of electrons transferred, h is the Planck's constant, c is the speed of light, I is the light intensity (74 mW·cm^{-2}), A is the irradiation area (ca. 9.6 cm^2), and λ is the wavelength of the irradiation light (365 nm).

Computational Method: Density functional theory calculations of methane adsorption and conversion on PdO were carried out using CP2K software.[48] Perdew-Burke-Ernzerhof (PBE) functional[49] was used, with Grimme's D3 correction[50] to describe dispersion interactions. Double-ζ valence polarized (DZVP) basis sets[51] were used in combination with Goedecker–Teter–Hutter (GTH) pseudopotentials;[52] the number of valence electrons was 18 for Pd, 6 for O, 1 for H and 4 for C. Periodic slabs of PdO exposed the (101) surface, which was reported to be the most reactive PdO surface for C-H activation.[53] The slabs had 6 repeat layers (12 atomic layers) and a 2 × 2 extended surface unit cell (48 Pd and O atoms per cell). The bottom two repeat layers were fixed, and the remaining layers and the adsorbate were allowed to optimize with the convergence criteria of 3×10^{-3} Bohr for the maximum geometry change, 4.5×10^{-4} Ha $Bohr^{-1}$ for the maximum force, 1.5×10^{-3} Bohr for the root mean square geometry change, and 3×10^{-4} Ha $Bohr^{-1}$ for the root mean square force. Transition state search was carried out using the Nudged Elastic Band (NEB) method,[54] to find the lowest-energy path along a sequence of steps from the reactant to the transition state. Eight replicas along the path were used, with the convergence criteria of 1×10^{-3} Ha $Bohr^{-1}$ for the maximum force and 4×10^{-3} Ha $Bohr^{-1}$ for the root mean square force. The highest-energy image along the path was taken to be the transition state. Geometry optimizations and NEB calculations were carried out both for the neutral surface/adsorbate system, and for the surface/adsorbate system with a +1 charge. DDEC charges on atoms[55] were calculated using Chargemol program[56] from CP2K-calculated electron density cube files.

Supporting Information

Supporting Information is available from the Wiley Online Library or from the author.

Acknowledgements

The authors acknowledge the NSFC project (Grant No: 22250710677) and Beijing Municipal Project (C2022007). The work is also supported by Tsinghua University Initiative Scientific Research Program and UK EPSRC (EP/ S018204/2). The authors also thank Prof. Dengwei Jing for TEM measurements.

Conflict of Interest

The authors declare no conflict of interest.

Author Contributions

J.Y. and L.X. contributed equally to this work. All authors have given approval to the final version of the manuscript.

Data Availability Statement

The data that support the findings of this study are available in the supplementary material of this article.

Keywords

chemical cycle process, ethane synthesis, flow reactors, methane, photocatalysis

Received: September 13, 2024
Revised: November 19, 2024
Published online:

[1] N. J. Gunsalus, A. Koppaka, S. H. Park, S. M. Bischof, B. G. Hashiguchi, R. A. Periana, *Chem. Rev.* **2017**, *117*, 8521.
[2] X. Li, C. Wang, J. Tang, *Nat. Rev. Mater.* **2022**, *7*, 617.
[3] H. Song, X. Meng, Z.-J. Wang, H. Liu, J. Ye, *Joule* **2019**, *3*, 1606.
[4] P. Zhang, J. Li, H. Huang, X. Sui, H. Zeng, H. Lu, Y. Wang, Y. Jia, J. A. Steele, Y. Ao, M. B. J. Roeffaers, S. Dai, Z. Zhang, L. Wang, X. Fu, J. Long, *J. Am. Chem. Soc.* **2024**, *146*, 24150.
[5] P. Mars, D. W. van Krevelen, *Chem. Eng. Sci.* **1954**, *3*, 41.
[6] L. Yu, W. Zhou, Z. Luo, H. Wang, W. Liu, K. Yin, *Adv. Sustainable Syst.* **2020**, *4*, 2000099.
[7] W. Sun, G. Zhao, Y. Gao, J. Si, Y. Liu, Y. Lu, *Appl. Catal., B: Environ.* **2022**, *304*, 120948.
[8] C. Jiang, S. J. A. Moniz, A. Wang, T. Zhang, J. Tang, *Chem. Soc. Rev.* **2017**, *46*, 4645.
[9] E. Gong, S. Ali, C. B. Hiragond, H. S. Kim, N. S. Powar, D. Kim, H. Kim, S.-I. In, *Energy Environ. Sci.* **2022**, *15*, 880.
[10] M. Ravi, M. Ranocchiari, J. A. van Bokhoven, *Angew. Chem., Int. Ed.* **2017**, *56*, 16464.
[11] X. Yu, V. L. Zholobenko, S. Moldovan, D. Hu, D. Wu, V. V. Ordomsky, A. Y. Khodakov, *Nat. Energy* **2020**, *5*, 511.
[12] S. Song, H. Song, L. Li, S. Wang, W. Chu, K. Peng, X. Meng, Q. Wang, B. Deng, Q. Liu, Z. Wang, Y. Weng, H. Hu, H. Lin, T. Kako, J. Ye, *Nat. Catal.* **2021**, *4*, 1032.
[13] K. Wenderich, G. Mul, *Chem. Rev.* **2016**, *116*, 14587.
[14] N. Nunotani, N. Moriyama, K. Matsuo, N. Imanaka, *ACS Appl. Mater. Interfaces* **2017**, *9*, 40344.
[15] J. Xue, Y. Chen, Y. Wei, A. Feldhoff, H. Wang, J. Caro, *ACS Catal.* **2016**, *6*, 2448.
[16] S. Wu, X. Tan, J. Lei, H. Chen, L. Wang, J. Zhang, *J. Am. Chem. Soc.* **2019**, *141*, 6592.
[17] S. P. Singh, A. Yamamoto, E. Fudo, A. Tanaka, H. Kominami, H. Yoshida, *ACS Catal.* **2021**, *11*, 13768.
[18] Y. Chai, S. Tang, Q. Wang, Q. Wu, J. Liang, L. Li, *Appl. Catal., B: Environ.* **2023**, *338*, 123012.
[19] C. Wang, K. Wang, Y. Feng, C. Li, X. Zhou, L. Gan, Y. Feng, H. Zhou, B. Zhang, X. Qu, H. Li, J. Li, A. Li, Y. Sun, S. Zhang, G. Yang, Y. Guo, S. Yang, T. Zhou, F. Dong, K. Zheng, L. Wang, J. Huang, Z. Zhang, X. Han, *Adv. Mater.* **2021**, *33*, 2003327.
[20] K. Shah, R. Dai, M. Mateen, Z. Hassan, Z. Zhuang, C. Liu, M. Israr, W.-C. Cheong, B. Hu, R. Tu, C. Zhang, X. Chen, Q. Peng, C. Chen, Y. Li, *Angew. Chem., Int. Ed.* **2022**, *61*, 202114951.
[21] Y. Tong, P. Chen, T. Zhou, K. Xu, W. Chu, C. Wu, Y. Xie, *Angew. Chem., Int. Ed.* **2017**, *56*, 7121.
[22] H. Song, X. Meng, S. Wang, W. Zhou, S. Song, T. Kako, J. Ye, *ACS Catal.* **2020**, *10*, 14318.
[23] S. Shen, J. Chen, M. Wang, X. Sheng, X. Chen, X. Feng, S. S. Mao, *Prog. Mater. Sci.* **2018**, *98*, 299.
[24] S. Chen, S. Li, R. You, Z. Guo, F. Wang, G. Li, W. Yuan, B. Zhu, Y. Gao, Z. Zhang, H. Yang, Y. Wang, *ACS Catal.* **2021**, *11*, 5666.
[25] F. Huang, J. Chen, W. Hu, G. Li, Y. Wu, S. Yuan, L. Zhong, Y. Chen, *Appl. Catal., B: Environ.* **2017**, *219*, 73.
[26] J. W. M. Jacobs, *J. Phys. Chem.* **1986**, *90*, 6507.
[27] X. Li, J. Xie, H. Rao, C. Wang, J. Tang, *Angew. Chem., Int. Ed.* **2020**, *59*, 19702.
[28] L. Wang, W. Zhang, X. Zheng, Y. Chen, W. Wu, J. Qiu, X. Zhao, X. Zhao, Y. Dai, J. Zeng, *Nat. Energy* **2017**, *2*, 869.
[29] D. C. Hurum, A. G. Agrios, S. E. Crist, K. A. Gray, T. Rajh, M. C. Thurnauer, *J. Electron Spectrosc. Relat. Phenom.* **2006**, *150*, 155.
[30] K. Komaguchi, H. Nakano, A. Araki, Y. Harima, *Chem. Phys. Lett.* **2006**, *428*, 338.
[31] T. Hirakawa, H. Kominami, B. Ohtani, Y. Nosaka, *J. Phys. Chem. B* **2001**, *105*, 6993.
[32] D. V. Glyzdova, E. V. Khramov, N. S. Smirnova, I. P. Prosvirin, A. V. Bukhtiyarov, M. V. Trenikhin, T. I. Gulyaeva, A. A. Vedyagin, D. A. Shlyapin, A. V. Lavrenov, *Appl. Surf. Sci.* **2019**, *483*, 730.
[33] H. Yu, K. Wada, T. Fukutake, Q. Feng, S. Uemura, K. Isoda, T. Hirai, S. Iwamoto, *Catal. Today* **2021**, *375*, 410.
[34] Z. Li, X. Pan, Z. Yi, *J. Mater. Chem. A* **2019**, *7*, 469.
[35] A. Hu, J.-J. Guo, H. Pan, Z. Zuo, *Science* **2018**, *361*, 668.
[36] K. Ramasesha, L. De Marco, A. Mandal, A. Tokmakoff, *Nat. Chem.* **2013**, *5*, 935.
[37] A. Levin, C. F. Meyer, *J. Opt. Soc. Am.* **1928**, *16*, 137.
[38] M. V. Sopinskyy, V. S. Khomchenko, V. V. Strelchuk, A. S. Nikolenko, G. P. Olchovyk, V. V. Vishnyak, V. V. Stonis, *Nanoscale Res. Lett.* **2014**, *9*, 182.
[39] X. Chen, X. Wang, D. Fang, *Fuller. Nanotub. Carbon Nanostructures* **2020**, *28*, 1048.
[40] S. Wu, X. Tan, J. Lei, H. Chen, L. Wang, J. Zhang, *J. Am. Chem. Soc.* **2019**, *141*, 6592.
[41] L. Luo, L. Fu, H. Liu, Y. Xu, J. Xing, C.-R. Chang, D.-Y. Yang, J. Tang, *Nat. Commun.* **2022**, *13*, 2930.
[42] H. Idriss, *Surf. Sci.* **2021**, *712*, 121894.
[43] S. Wang, B. Ge, Z. Yang, H. Zhang, Q. Yang, C. Hu, X. Bao, P. Yuan, *ACS Catal.* **2024**, *14*, 1.
[44] A. Barrera, S. Fuentes, G. Díaz, A. Gómez-Cortés, F. Tzompantzi, J. C. Molina, *Fuel* **2012**, *93*, 136.
[45] G. Lapisardi, L. Urfels, P. Gélin, M. Primet, A. Kaddouri, E. Garbowski, S. Toppi, E. Tena, *Catal. Today* **2006**, *117*, 564.
[46] B. Yue, R. Zhou, Y. Wang, X. Zheng, *J. Mol. Catal. A: Chem.* **2005**, *238*, 241.
[47] Y. H. Chin, C. Buda, M. Neurock, E. Iglesia, *J. Am. Chem. Soc.* **2013**, *135*, 15425.
[48] T. D. Kühne, M. Iannuzzi, M. Del Ben, V. V. Rybkin, P. Seewald, F. Stein, T. Laino, R. Z. Khaliullin, O. Schütt, F. Schiffmann, D. Golze, J. Wilhelm, S. Chulkov, M. H. Bani-Hashemian, V. Weber, U. Borštnik, M. Taillefumier, A. S. Jakobovits, A. Lazzaro, H. Pabst, T. Müller, R. Schade, M. Guidon, S. Andermatt, N. Holmberg, G. K. Schenter, A. Hehn, A. Bussy, F. Belleflamme, G. Tabacchi, et al., *J. Chem. Phys.* **2020**, *152*, 194103.
[49] J. P. Perdew, K. Burke, M. Ernzerhof, *Phys. Rev. Lett.* **1996**, *77*, 3865.
[50] S. Grimme, J. Antony, S. Ehrlich, H. Krieg, *J. Chem. Phys.* **2010**, *132*, 154104.

[51] J. VandeVondele, J. Hutter, *J. Chem. Phys.* **2007**, *127*, 114105.
[52] S. Goedecker, M. Teter, J. Hutter, *Phys. Rev. B* **1996**, *54*, 1703.
[53] Y.-H. Chin, C. Buda, M. Neurock, E. Iglesia, *J. Am. Chem. Soc.* **2013**, *135*, 15425.
[54] G. Henkelman, B. P. Uberuaga, H. Jónsson, *J. Chem. Phys.* **2000**, *113*, 9901.
[55] N. G. Limas, T. A. Manz, *RSC Adv.* **2018**, *8*, 2678.
[56] T. A. Manz, *RSC Adv.* **2017**, *7*, 45552.